PHYSICAL REVIEW FLUIDS **9**, L081601 (2024)

Letter

Gravito-capillary trapping of pendant droplets under wet uneven surfaces

Etienne Jambon-Puillet

LadHyX, CNRS, École Polytechnique, Institut Polytechnique de Paris, 91120 Palaiseau, France

(Received 13 February 2024; accepted 16 July 2024; published 7 August 2024)

Pendant drops spontaneously appear on the underside of wet surfaces through the Rayleigh-Taylor instability. These droplets are connected to a thin liquid film with which they exchange liquid and are thus very mobile. Here, using experiments, numerical simulations, and theory, I show that pendant drops sliding under a slightly tilted wet substrate can get stuck on topographic defects, despite their lack of contact line. Instead, this trapping has a gravito-capillary origin: liquid has to move up or down and the interface has to deform for the drop to pass the defect. I propose a semianalytical model for arbitrary substrate topographies that matches the trapping force observed, without any fitting parameter. I finally demonstrate how to harness this topography induced force to guide pendant drops on complex paths and expect it to be relevant for other contact line free systems.

DOI: 10.1103/PhysRevFluids.9.L081601

A thin liquid film covering the underside of a surface will spontaneously destabilize and form an array of pendant droplets [1,2]. This process can be easily observed in kitchens, bathrooms, and other everyday life situations [e.g. Fig. 1(a)], has important consequences for many applications; it can impair the quality of coatings [3] or, conversely, be harnessed to pattern surfaces [4,5], impacts geomorphological processes [6–8], and can be detrimental to engineering constructs with wet surfaces [9,10]. For these reasons, the Rayleigh-Taylor instability in thin viscous films has been thoroughly investigated [1,2,11–13] and various approaches to avoid it have been developed and rationalized with linear stability analysis [14–20].

The late-time, nonlinear dynamics of the fully formed pendant droplets has received less attention [21,22]. A distinctive feature of these drops is their absence of contact line, they are connected to a thinner macroscopic film with which they continuously exchange liquid. This makes them very mobile and under smooth, and uniformly wet substrates, any tilt or perturbation will set them in motion and alter their growth rate [21,22]. However, surfaces in most practical situations are uneven. For instance, the ceiling of caves is covered by speleotherms [8], and patterned surfaces have been used to control the local thickness of coatings [4]. For sessile drops, surface roughness usually hinders their motion by pinning their contact line [23–26]. Since pendant drops on the underside of wet surfaces lack a contact line, the effect of topographical defects on their motion is unclear.

In this Letter, using experiments, numerical simulations, and theory, I show that topographic defects can capture a single pendant drop sliding under a slightly tilted uniformly wet substrate. The defect generates a trapping force which stops the drop if the inclination angle is too low. This critical inclination angle depends on the defect dimensions, and not on the drop size or underlying film thickness. I derive a gravito-capillary model that yields a semianalytical prediction for this topography induced force and the critical angle that matches experiments and simulations without any fitting parameters. Locally, as the drop slides on the defect, fluid is displaced vertically and the interface is distorted, creating potential energy variations responsible for the force. Finally, I demonstrate how to use this trapping force to guide the motion of pendant drops using the substrate topography. This gravito-capillary force being generic, I expect these results to be relevant for

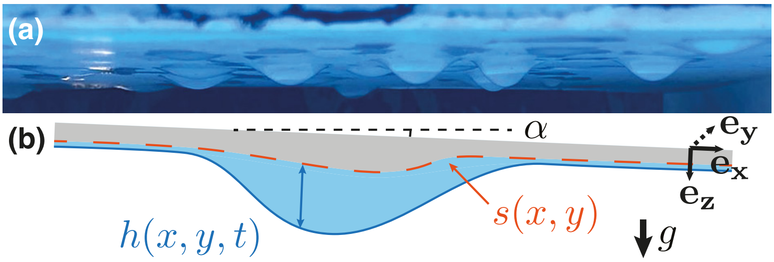

FIG. 1. (a) Several pendant droplets on the ceiling of a swimming pool skimmer. Drop diameters $\sim$2 cm. (b) Schematic of a thin liquid film of thickness $h(x, y, t)$ that contains a pendant drop sliding under a surface with topography $s(x, y)$, inclined by an angle α.

other systems lacking a contact line such as drops on liquid infused surfaces or bubbles under walls.

The problem considered here is schematized in Fig. 1(b). The underside of a solid with a nonflat topography, slightly tilted by an angle α, is wet by a thin layer of liquid over which lies a pendant drop. Experimentally, I create controlled surface defects by milling PMMA plates and use silicone oil (density $\rho = 971\,\mathrm{kg/m^3}$, surface tension $\gamma = 20.5$ mN/m, viscosity $\eta = 1$ Pa.s) as a fluid. Prewetting is achieved by spin-coating oil on the substrate which results in a uniform film thickness h_0, except close to the defects [28,29]. The substrate is then mounted upside down to a rotation stage. A single pendant droplet of amplitude $A_0 \sim \ell_c$ is generated by adding oil on the spin-coated film with a syringe. Here $\ell_c = \sqrt{\gamma/(\rho g)} \approx 1.47$ mm denotes the capillary length with g the gravitational acceleration. The substrate is finally tilted by an angle α and the drop dynamics is recorded (see Sec I A of the Supplemental Material [27]). Note that the spin-coated film is sufficiently thin and smooth to neglect the growth of the Rayleigh-Taylor instability over the timescale of the experiment, i.e., $t_{\mathrm{exp}} \ll 12\tau$ with $\tau = \eta\gamma/(h_0^3\rho^2 g^2 \cos^2\alpha)$ [4] (see Sec. I A of the SM [27]).

I start by investigating the simplest topographic defect, a one-dimensional step of height h_s that spans the full width of the substrate see the inset of Fig. 2(a)]. Figure 2(a) shows two chronophotographies of a pendant drop sliding under the same prewet surface with a step defect, at two slightly different inclination angles. Below a critical inclination angle α_c, the pendant drop is stopped by the step. Above α_c, the drop is slowed down but is able to pass (see also movie S1 and Sec. II C of the SM [27] for a discussion on the drop dynamics). The step thus displays a pinninglike force that hinders the drop motion. Note that this trapping force is directional. In the experiment shown in Fig. 2(a), the drop climbs up the step. Inverting the step such that the drop descends it instead results in the drop accelerating over the step. In principle, the critical angle, and thus the trapping force, can depend on the droplet size A, the prewetting thickness h_0, the step height h_s, and its sharpness δ [see the inset of Fig. 2(a)]. To explore this large parameter space efficiently, I turn to numerical simulations.

Taking advantage of the problem thinness, I use the lubrication approximation to solve the steady Stokes flow in the film of thickness $h(x, y, t)$ over an uneven substrate of profile $s(x, y)$ inclined by an angle α [see Fig. 1(b)]. In the Cartesian frame aligned with the substrate, this yields a parabolic flow profile $\mathbf{u} = \frac{(z-s)^2-2h(z-s)}{2\eta}[\nabla P - \rho g \sin\alpha \mathbf{e_x}]$ with $\mathbf{u} = (u_x, u_y)$ [29]. The thin-film equation is then obtained by applying mass conservation over a film element $\partial_t h = -\nabla\cdot\mathbf{q}$ with $\mathbf{q} = \int_s^{s+h}\mathbf{u}dz = \frac{-h^3}{3\eta}[\nabla P - \rho g \sin\alpha \mathbf{e_x}]$ the local flowrate. Inserting the capillary and gravitational pressures $P = p_0 - \rho g \cos\alpha(h + s - z) - \gamma\kappa$, with κ the interface curvature, yields Eq. (S1) [1,8,13,21,22,28–30]. After rescaling $\{x, y\}$ with $\ell_c/\sqrt{\cos\alpha}$, $\{h, s\}$, with h_0 the initial uniform thickness far from the

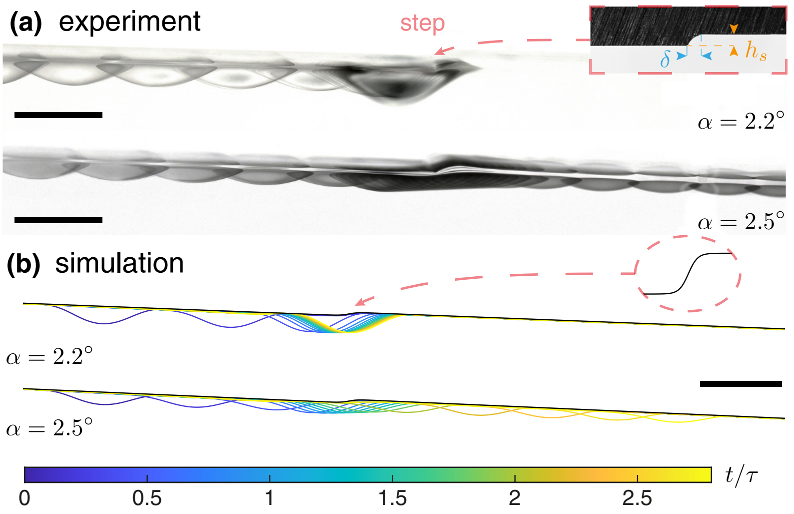

FIG. 2. (a) Side view chronophotography of two experiments showing pendant drops of initial size $A/\ell_c = \{1, 0.7\}$ sliding under a surface with a step of height $h_s = 330$ μm and sharpness $\delta \approx 400$ μm (see inset), prewet with a film of thickness $h_0 \approx 60$ μm, at two different inclination angles $\alpha = \{2.2, 2.5\}$ deg. The images include the drop reflection on the wet substrate. Scale bar 5 mm, time interval 2 min. (b) Numerical replication of the experiment in (a) (identical parameters except for the step sharpness $\delta = \ell_c$). The profiles are slices through the center of the 3D simulations, color codes the time, and the scale bar is 5 ℓ_c. The inset shows the step dilated vertically by a factor of 5. See also movies S1, S2, and Sec. II C of the SM for a discussion on the drop dynamics [27].

drop and t with τ, it reads in dimensionless form

$$\frac{\partial \bar{h}}{\partial \bar{t}} + \widetilde{\alpha}\bar{h}^2 \frac{\partial \bar{h}}{\partial \bar{x}} + \frac{1}{3}\bar{\nabla}\cdot[\bar{h}^3\bar{\nabla}(\bar{h}+\bar{s}) + \bar{h}^3\bar{\nabla}\bar{\kappa}] = 0,$$

$$\text{with} \quad \bar{\kappa} = \bar{\nabla}\cdot\left[\frac{\bar{\nabla}(\bar{h}+\bar{s})}{\sqrt{1+(h_0\sqrt{\cos\alpha}/\ell_c)^2(\bar{\nabla}(\bar{h}+\bar{s}))^2}}\right]. \qquad (1)$$

Here a bar indicates rescaled variables, and the parameter $\widetilde{\alpha} = (\ell_c \tan\alpha)/(h_0\sqrt{\cos\alpha})$ accounts for the substrate inclination (for small angles $\widetilde{\alpha} \approx \ell_c\alpha/h_0$). I numerically solve Eq. (1) with COMSOL, using the initial condition $\bar{h}(\bar{x}, \bar{y}, 0) = 1 + \bar{h}_d(\bar{x}, \bar{y})$, where $h_d(x, y)$ is the profile of a static pendant drop of amplitude A_0 solved independently (see Sec. I B of the SM [27]).

In Fig. 2(b), I show a numerical reproduction of the experiment shown in panel (a), where the step is idealized as a hyperbolic tangent: $s_{1d}(x, y) = (h_s/2)(1 - \tanh(2x/\delta))$ (see also movie S2 [27]). There is a critical inclination angle to pass the step α_c which matches the experimental one, despite the different step shape and sharpness. Varying the liquid parameters, i.e., the drop initial amplitude ($0.65 < A_0/\ell_c < 1.42$) and the prewetting film thickness ($0.04 < h_0/\ell_c < 0.08$), I observe an influence on the drop speed and growth rate, as previously shown on flat surfaces [21,22]. Yet, surprisingly, they have no impact on the critical angle to pass the step α_c. The topography, however, does impact the capture process. For sharp enough steps, $\delta \lesssim R$ with $R \approx 3.58\ell_c$ the drop radius [22], the critical angle appears independent of the sharpness (see Fig. S4 [27]), while for very smooth steps $\delta \gtrsim R$, it varies with it (see Fig. S5a [27]). The step height h_s affects α_c in all cases: the higher the step, the larger the critical angle. The smooth step regime ($\delta \gtrsim R$) can be understood

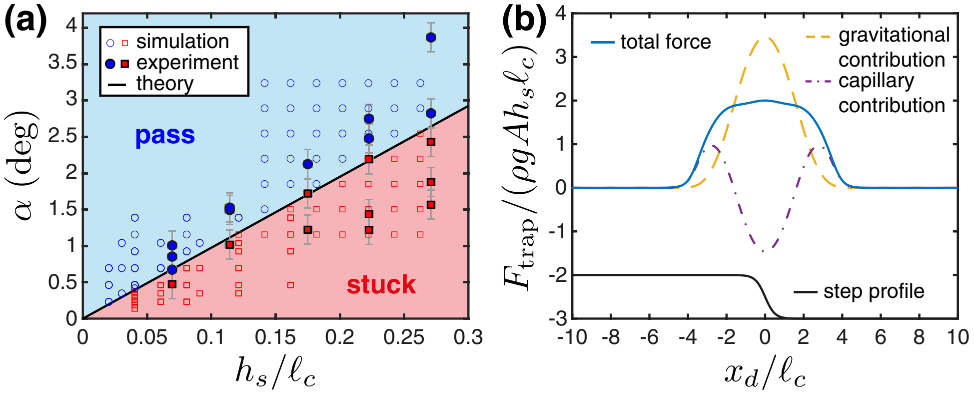

FIG. 3. (a) Phase diagram for the drop capture by a sharp step with $\delta < 2\ell_c$ (see legend). The black line and background colors are Eq. (4): $\alpha_c = 0.1703 h_s/\ell_c$. (b) Dimensionless trapping force for a drop of size $A = \ell_c$ on a sharp step ($\delta = \ell_c$, black solid curve with abscissa x/ℓ_c). The gravitational and capillary contributions to the total force are highlighted (see legend).

as a local slope variation such that $\alpha_c \sim h_s/\delta$ (see Sec. II A of the SM [27]). In the following, I focus on the more complex sharp regime and show in Fig. 3(a) a phase diagram for the drop behavior combining simulations where all parameters are varied while keeping $\delta < 2\ell_c$ (points for different values of δ, h_0, and A_0 are superimposed). I observe a linear relationship $\alpha_c \propto h_s$, which is confirmed by experiments done on five milled steps of different heights with $h_0 \approx 60$ μm and $0.55 < A_0/\ell_c < 1.07$, also shown in Fig. 3(a).

Since there is no contact line, the origin of this trapping force has to be gravito-capillary. As the drop advances on the step, locally some of the drop volume is lifted up, which costs gravitational energy and its surface may deform which costs capillary energy [31]. Both effects combined create a potential energy barrier responsible for the trapping. While estimating the capillary energy contribution is not straightforward, one can easily get a scaling for the gravitational one. In the sharp limit, the volume to be lifted over a distance h_s is maximum when the apex of the drop reaches the step and can be estimated as $\mathrm{d}V \sim 2AR\mathrm{d}x$. The energy cost is thus $\mathrm{d}E_g \sim -\rho g(2AR\mathrm{d}x)h_s$ and the force is $F_{\text{trap}} = -\mathrm{d}E_g/\mathrm{d}x \sim \rho g A R h_s$. Neglecting the droplet growth during the step crossing, the surface inclination generates a driving force $F_d = \rho g V \sin\alpha$ with $V \sim AR^2$. Equating the two yields for small angles $\alpha_c \sim h_s/R$. Viscous effetcs are neglected here since close to the critical angle the drop velocity approaches zero. They are, however, important to determine the drop dynamic above α_c (see Sec. II C of the SM [27]). Finally, the radius of pendant drops being $R \approx 3.58\ell_c$ [22], I recover the scaling observed in Fig. 3(a). The prefactor of this simple scaling argument, however, is not correct since it neglects the capillary contribution which I expect to be significant given that pendant drops have a size comparable to ℓ_c. To go beyond, I have to compute the total energy barrier that also includes the capillary contribution.

In the reference frame aligned with the surface [see Fig. 1(b)], the gravitational energy has two contributions: one from the slope responsible for the driving force $F_d = \rho g V \sin\alpha$ and one from the surface unevenness $E_g = \iiint \rho g \cos(\alpha) z \,\mathrm{d}x\mathrm{d}y\mathrm{d}z = \iint \frac{1}{2}\rho g \cos(\alpha)((h+s)^2 - s^2)\,\mathrm{d}x\mathrm{d}y$ (see Sec. I C of the SM [27]). The capillary energy is $E_c = \iint \gamma \sqrt{1 + (\frac{\partial(h+s)}{\partial x})^2 + (\frac{\partial(h+s)}{\partial y})^2}\mathrm{d}x\mathrm{d}y$. To compute the total energy $E = E_g + E_c$ as a function of the drop position (x_d, y_d) with respect to the topography, I neglect any variations in film or drop thickness and assume that $h(x, y) = h_0 + h_d(x - x_d, y - y_d)$. Using the small slope approximation, and assuming a small inclination angle yields (see Sec. I C of the SM [27])

$$\frac{E(x_d, y_d)}{\rho g} = E_{g0} + E_{c0} + \iint h_d(x - x_d, y - y_d) s(x, y) \mathrm{d}x\mathrm{d}y$$

$$+ \ell_c^2 \iint \left(\frac{\partial h_d}{\partial x}\bigg|_{\substack{x-x_d \\ y-y_d}} \frac{\partial s}{\partial x} + \frac{\partial h_d}{\partial y}\bigg|_{\substack{x-x_d \\ y-y_d}} \frac{\partial s}{\partial y} \right) \mathrm{d}x\mathrm{d}y. \tag{2}$$

Here E_{g0} and E_{c0} are constant terms with respect to the drop position. The prewetting thickness h_0 enters in these terms and does not participate to the energy barrier. Rescaling $\{x, y\}$ with the capillary length ℓ_c, h_d with the drop amplitude A, and s with the topography scale h_s, the trapping force is then

$$\frac{\mathbf{F}_{\text{trap}}(\hat{x_d}, \hat{y_d})}{\rho g A h_s \ell_c} = -\hat{\nabla}\left[(\hat{h_d} * \hat{s}) + \left(\frac{\partial \hat{h_d}}{\partial \hat{x}} * \frac{\partial \hat{s}}{\partial \hat{x}} \right) + \left(\frac{\partial \hat{h_d}}{\partial \hat{y}} * \frac{\partial \hat{s}}{\partial \hat{y}} \right) \right]. \tag{3}$$

Here $\hat{}$ denotes dimensionless variables, and $(*)$ the convolution operator $(f * g)(x_d, y_d) = \iint f(x - x_d, y - y_d) g(x, y) \mathrm{d}x\mathrm{d}y$. While not fully analytical, Eq. (3) can be integrated very efficiently by computing the 2D convolutions in Fourier space.

Performing this calculation for the steps $\hat{s}_{1d}$, I obtain the theoretical trapping force shown in Fig. 3(b). The capillary contribution partially counteracts the gravitational one and the trapping force is maximum when the drop apex sits on the step. Extracting this maximum and equating it with the drop driving force $F_d \approx \rho g V \alpha$, I obtain the critical inclination angle for the drop to pass the step

$$\alpha_c = c_{1d}\frac{h_s}{\ell_c}, \quad \text{with} \quad c_{1d} = \frac{A\ell_c^2}{V} \max_{\hat{x_d}, \hat{y_d}} \left(-\frac{\partial}{\partial \hat{x}}\left[(\hat{h_d} * \hat{s}_{1d}) + \left(\frac{\partial \hat{h_d}}{\partial \hat{x}} * \frac{\partial \hat{s}_{1d}}{\partial \hat{x}} \right) \right] \right) \approx 0.1703. \tag{4}$$

The prefactor c_{1d} is almost constant. It varies very slowly with δ in the sharp limit (see Fig. S5 [27]) and is almost independent of the choice of static pendant drop h_d to convolve (see Fig. S6a [27]). This is due to the near self-similarity of pendant drops: the rescaled profiles $\hat{h_d}$ used in the model are nearly identical (see Fig. S3d and Sec. II B of the SM [27]). In Fig. 3(a), I overlay the result of Eq. (4) on numerical and experimental data and find an excellent agreement without any fitting parameter. I further test the model to see if it can capture the transition between sharp and smooth steps ($\delta > 2\ell_c$) in Fig. S5 [27] and again find a very good agreement.

I now extend the analysis to bidimensional steps, or bumps, $s_{2d}(x, y) = \frac{h_s}{2}(1 - \tanh[\frac{2\sqrt{x^2+y^2}-w}{\delta} - 1])$ which introduce the bump width w as a new parameter. Note that the width w is defined around the top of the bump rather than at midheight: $s_{2d}(w/2, 0) \approx 0.88 h_s$. This choice allows to compare the numerical results with milled experimental surface where the width is defined at the top in the milling process. As a results, the surface $s_{2d}(x, y)$ departs from a smooth bump for $w < \delta$ and is nonflat for $w = 0$ (see Fig. S3a [27]). I run numerical simulations keeping $\delta = \ell_c$ fixed to remain in the sharp regime, and $w \lesssim 2R$ since bumps much wider than the drop will reduce to 1D steps. Qualitatively, bumps behave similarly to steps (see movie S3 [27]). For small enough inclination angles, the drop is captured by the bump while for larger angles it is able to pass over it. However, the capture here is omnidirectional, as expected from the symmetry of the defect. Turning the bump into a trough ($h_s < 0$) on the opposite repels the drop (see movie S3 [27]).

I construct a multidimensional phase diagram from which I extract the critical angle α_c shown in Fig. 4(a) as a function of the bump height h_s and width w (color coded). As shown, wider and taller bumps generate a larger critical angle. The prewetting film thickness h_0 still has no effect on the observed critical capture angle while the drop size A has a negligible impact. Equation (3) predicts a $\mathbf{F}_{\text{trap}} \propto h_s$. Thus, in Fig. 4(b) I plot the critical angle rescaled by the bump height $\alpha_c \ell_c / h_s$ as a function of the dimensionless bump width w/ℓ_c and observe a good collapse of the numerical data.

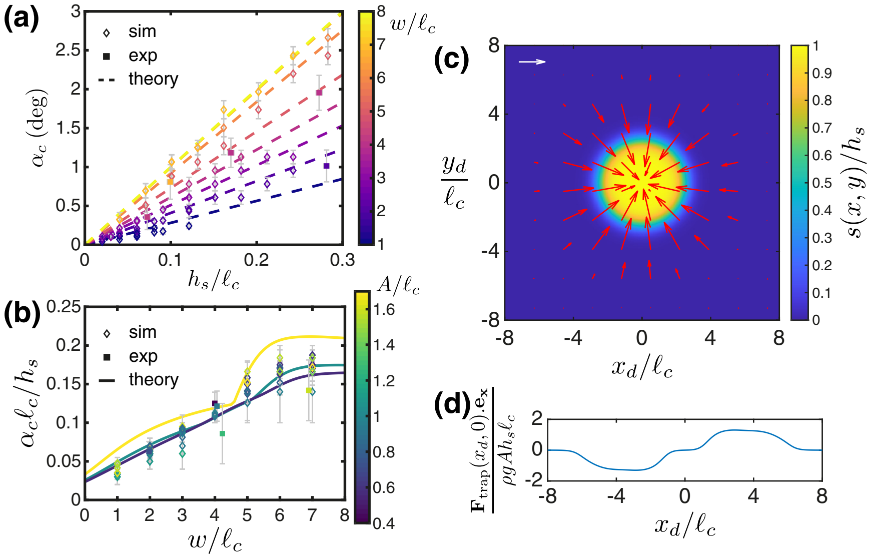

FIG. 4. (a) Critical angle α_c as a function of the dimensionless bump height h_s/ℓ_c and width w/ℓ_c (color coded). The model, i.e., Eq. (5), is shown as dashed lines for integer values of w/ℓ_c and a pendant drop of size $A = \ell_c$. (b) Reduced critical angle $\alpha_c\ell_c/h_s$ as a function of the dimensionless bump width w/ℓ_c. Same data as (a), the color represents the drop dimensionless height A/ℓ_c. (c) Dimensionless trapping force field $\mathbf{F}_{\text{trap}}/(\rho g A h_s \ell_c)$ (arrows) for a bump of width $w/\ell_c = 4$ (background color with axes $\{x, y\}/\ell_c$) and a pendant drop of size $A = \ell_c$. The white arrow act as a scale with a magnitude of one. (d) Slice of the data in (c) through the center of the defect.

I compare these numerical results to experiments with five milled surfaces (see Sec. I A of the SM and Figs. S1d and f [27]), also shown in Figs. 4(a) and 4(b). The experimental critical angles are in line with the numerics.

To understand the width dependence, I use Eq. (3), as in the step case, but now with $\hat{s}_{2d}(\hat{x}, \hat{y})$. I show in Figs. 4(c) and 4(d) the theoretical force field for a pendant drop of size $A = \ell_c$ on a bump of width $w/\ell_c = 4$. The bump defect acts as an omnidirectional attractor for the drop with a range $\sim w/2 + R$. The maximum trapping force does not occur at the center of the bump but on an annulus, in line with the observed off-centered drop capture (see movie S3 and Figs. S1d–f [27]). Equating this maximum trapping force in the slope direction x with the driving force, I calculate the critical angle:

$$\alpha_c = c_{2d}\left(\frac{w}{\ell_c}\right)\frac{h_s}{\ell_c},$$

$$\text{with}\quad c_{2d}\left(\frac{w}{\ell_c}\right) = \frac{A\ell_c^2}{V}\max_{\hat{x}_d,\hat{y}_d}\left(-\frac{\partial}{\partial \hat{x}}\left[(\hat{h_d} * \hat{s}_{2d}) + \left(\frac{\partial \hat{h_d}}{\partial \hat{x}} * \frac{\partial \hat{s}_{2d}}{\partial \hat{x}}\right) + \left(\frac{\partial \hat{h_d}}{\partial \hat{y}} * \frac{\partial \hat{s}_{2d}}{\partial \hat{y}}\right)\right]\right). \quad (5)$$

I compare Eq. (5) to simulations and experiments in Figs. 4(a) and 4(b) and find a good agreement. The width function $c_{2d}(w/\ell_c)$ increases with the bump width until it eventually plateaus around the step value c_{1d} for bumps larger than the drop $w \gtrsim 2R$. As shown in Fig. 4(b), the influence of the pendant drop size A/ℓ_c, while still small, is more pronounced than in the step case. In particular, as the drop gets larger, $c_{2d}(w/\ell_c)$ develop kinks due to the competition of multiples maximas in the pinning force field $\mathbf{F}_{\text{trap}}$ (see Sec. II B of the SM [27]). This size dependence is not so clear

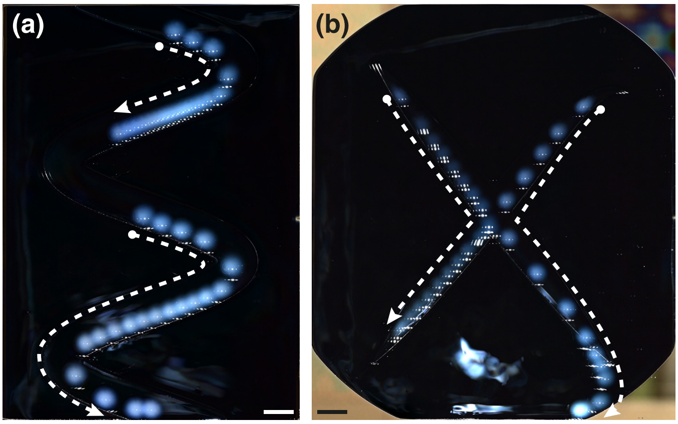

FIG. 5. Bottom view chronophotography of two pendant droplets sliding under a prewet tilted plate milled with an elevated path ($\alpha \approx 1$ deg from top to bottom, $h_0 \approx 44$ μm): sinusoidal in (a) and X shaped in (b) (see movie S4 [27]). Each droplet's trajectory is indicated by a white dashed arrow. White dye was used for visualization. Scale bars 1 cm, time interval 15 min.

in simulation data, perhaps because the drop profile shifts from its flat static case assumed in the model.

Now that I understand the gravito-capillary trapping force generated by elementary defects, I can design surfaces to guide pendant droplets along a chosen path. One can either use trenches that repel the drop, or elevate the surface along the desired path to attract the droplet [32]. The guiding element(s) width w and height h_s can be tuned using Fig. 4(b) or Eq. (3) to retain the drop on the path at the desired inclination angle. As a proof of concept, I mill a surface with an elevated sinusoidal path, of width $w = 12\,\text{mm}$ and height $h_s = 250$ μm (see Fig. S2 [27]). As shown in Fig. 5(a) and movie S4 [27], pendant droplets under this prewet surface inclined by $\alpha \approx 1$ deg follow the prescribed sinusoidal path. In Fig. 5(b) I show a more complex X shaped path that features a branching point ($h_s = 250$ μm, varying width, $\alpha \approx 1$ deg, see Fig. S2 [27]). Two drops traveling on the converging branches of the X will merge if they meet at the branching point, but will continue on their respective branch if they pass sequentially (see movie S4 [27]).

In summary, I have demonstrated that topographic defects impact the motion of pendant droplets on the underside of wet substrates, despite their lack of contact line. Using numerical simulations, experiments, and theory, I have shown that defects generate a gravito-capillary force capable of capturing a drop; for the drop to slide over the defect, some liquid has to change altitude and the liquid surface has to deform. I propose a model for the trapping force, Eq. (3), that predicts the critical capture angle observed in experiments and numerical simulations quantitatively without any fitting parameter. Finally, I show how to use these findings to design topographies that control the motion of pendant drops.

These results not only shed light on an unusual form of droplet capture but could also be harnessed to design surfaces that control the position and motion of pendant drops [4,5]. Besides, gravito-capillary trapping is relevant to thin film dynamics on natural nonsmooth surfaces and could affect the formation of some geomorphological patterns, like curtains and draperies in natural caves [8]. Finally, the trapping mechanism being generic, it should apply to other systems lacking a contact line such as sessile droplets on liquid infused surfaces [33] or nonwetting bubbles [34].

I thank T. Perrin and C. Hasson from the Drahi-X Novation Center for their help in milling the surfaces. I am grateful to P.G. Ledda, F. Gallaire, and P.-T. Brun for their feedback on the manuscript.

[1] S. G. Yiantsios and B. G. Higgins, Rayleigh–Taylor instability in thin viscous films, Phys. Fluids **1**, 1484 (1989).

[2] M. Fermigier, L. Limat, J. E. Wesfreid, P. Boudinet, and C. Quilliet, Two-dimensional patterns in Rayleigh-Taylor instability of a thin layer, J. Fluid Mech. **236**, 349 (1992).

[3] S. J. Weinstein and K. J. Ruschak, Coating flows, Annu. Rev. Fluid Mech. **36**, 29 (2004).

[4] J. Marthelot, E. F. Strong, P. M. Reis, and P.-T. Brun, Designing soft materials with interfacial instabilities in liquid films, Nat. Commun. **9**, 4477 (2018).

[5] E. Jambon-Puillet, M. Royer Piéchaud, and P.-T. Brun, Elastic amplification of the Rayleigh-Taylor instability in solidifying melts, Proc. Natl. Acad. Sci. USA **118**, e2020701118 (2021).

[6] N. Ribe, A. Davaille, and U. Christensen, Fluid dynamics of mantle plumes, in *Mantle Plumes: A Multidisciplinary Approach*, edited by J. R. R. Ritter and U. R. Christensen (Springer, Berlin, Heidelberg, 2007), pp. 1–48.

[7] U. Dutta, A. Baruah, and N. Mandal, Role of source-layer tilts in the axi-asymmetric growth of diapirs triggered by a Rayleigh–Taylor instability, Geophysical Journal International **206**, 1814 (2016).

[8] P. G. Ledda, G. Balestra, G. Lerisson, B. Scheid, M. Wyart, and F. Gallaire, Hydrodynamic-driven morphogenesis of karst draperies: Spatio-temporal analysis of the two-dimensional impulse response, J. Fluid Mech. **910**, A53 (2021).

[9] R. Kaita, L. Berzak, D. Boyle, T. Gray, E. Granstedt, G. Hammett, C. M. Jacobson, A. Jones, T. Kozub, H. Kugel, B. Leblanc, N. Logan, M. Lucia, D. Lundberg, R. Majeski, D. Mansfield, J. Menard, J. Spaleta, T. Strickler, J. Timberlake *et al.*, Experiments with liquid metal walls: Status of the lithium tokamak experiment, Fusion Eng. Des. **85**, 874 (2010).

[10] G. G. van Eden, V. Kvon, M. C. M. van de Sanden, and T. W. Morgan, Oscillatory vapour shielding of liquid metal walls in nuclear fusion devices, Nat. Commun. **8**, 192 (2017).

[11] L. Limat, P. Jenffer, B. Dagens, E. Touron, M. Fermigier, and J. Wesfreid, Gravitational instabilities of thin liquid layers: Dynamics of pattern selection, Physica D **61**, 166 (1992).

[12] H. N. Yoshikawa, C. Mathis, S. Satoh, and Y. Tasaka, Inwardly rotating spirals in a nonoscillatory medium, Phys. Rev. Lett. **122**, 014502 (2019).

[13] G. Lerisson, P. G. Ledda, G. Balestra, and F. Gallaire, Instability of a thin viscous film flowing under an inclined substrate: Steady patterns, J. Fluid Mech. **898**, A6 (2020).

[14] J. M. Burgess, A. Juel, W. D. McCormick, J. B. Swift, and H. L. Swinney, Suppression of dripping from a ceiling, Phys. Rev. Lett. **86**, 1203 (2001).

[15] V. Lapuerta, F. J. Mancebo, and J. M. Vega, Control of Rayleigh-Taylor instability by vertical vibration in large aspect ratio containers, Phys. Rev. E **64**, 016318 (2001).

[16] A. Alexeev and A. Oron, Suppression of the Rayleigh-Taylor instability of thin liquid films by the marangoni effect, Phys. Fluids **19**, 082101 (2007).

[17] R. Cimpeanu, D. T. Papageorgiou, and P. G. Petropoulos, On the control and suppression of the Rayleigh-Taylor instability using electric fields, Phys. Fluids **26**, 022105 (2014).

[18] P. H. Trinh, H. Kim, N. Hammoud, P. D. Howell, S. J. Chapman, and H. A. Stone, Curvature suppresses the Rayleigh-Taylor instability, Phys. Fluids **26**, 051704 (2014).

[19] P.-T. Brun, A. Damiano, P. Rieu, G. Balestra, and F. Gallaire, Rayleigh-Taylor instability under an inclined plane, Phys. Fluids **27**, 084107 (2015).

[20] G. Balestra, N. Kofman, P.-T. Brun, B. Scheid, and F. Gallaire, Three-dimensional Rayleigh–Taylor instability under a unidirectional curved substrate, J. Fluid Mech. **837**, 19 (2018).

[21] J. R. Lister, J. M. Rallison, and S. J. Rees, The nonlinear dynamics of pendent drops on a thin film coating the underside of a ceiling, J. Fluid Mech. **647**, 239 (2010).

[22] E. Jambon-Puillet, P. G. Ledda, F. Gallaire, and P.-T. Brun, Drops on the underside of a slightly inclined wet substrate move too fast to grow, Phys. Rev. Lett. **127**, 044503 (2021).

[23] J. F. Joanny and P. G. de Gennes, A model for contact angle hysteresis, J. Chem. Phys. **81**, 552 (1984).

[24] G. D. Nadkarni and S. Garoff, An investigation of microscopic aspects of contact angle hysteresis: Pinning of the contact line on a single defect, Europhys. Lett. **20**, 523 (1992).

[25] Y. V. Kalinin, V. Berejnov, and R. E. Thorne, Contact line pinning by microfabricated patterns: Effects of microscale topography, Langmuir **25**, 5391 (2009).

[26] J. Park and S. Kumar, Droplet sliding on an inclined substrate with a topographical defect, Langmuir **33**, 7352 (2017).

[27] See Supplemental Material at http://link.aps.org/supplemental/10.1103/PhysRevFluids.9.L081601 for experimental, numerical, and theoretical methods, additional results and discussion, as well as movies of the experiments and simulations. It also includes Ref. [35].

[28] L. E. Stillwagon and R. G. Larson, Leveling of thin films over uneven substrates during spin coating, Phys. Fluids **2**, 1937 (1990).

[29] P. H. Gaskell, P. K. Jimack, M. Sellier, H. M. Thompson, and M. C. T. Wilson, Gravity-driven flow of continuous thin liquid films on non-porous substrates with topography, J. Fluid Mech. **509**, 253 (2004).

[30] S. D. R. Wilson, The drag-out problem in film coating theory, J. Eng. Math. **16**, 209 (1982).

[31] R. Dangla, S. Lee, and C. N. Baroud, Trapping microfluidic drops in wells of surface energy, Phys. Rev. Lett. **107**, 124501 (2011).

[32] P. Abbyad, R. Dangla, A. Alexandrou, and C. N. Baroud, Rails and anchors: Guiding and trapping droplet microreactors in two dimensions, Lab Chip **11**, 813 (2011).

[33] T.-S. Wong, S. H. Kang, S. K. Y. Tang, E. J. Smythe, B. D. Hatton, A. Grinthal, and J. Aizenberg, Bioinspired self-repairing slippery surfaces with pressure-stable omniphobicity, Nature (London) **477**, 443 (2011).

[34] E. Esmaili, P. Shukla, J. D. Eifert, and S. Jung, Bubble impact on a tilted wall: Removing bacteria using bubbles, Phys. Rev. Fluids **4**, 043603 (2019).

[35] S. Preibisch, S. Saalfeld, J. Schindelin, and P. Tomancak, Software for bead-based registration of selective plane illumination microscopy data, Nature Methods **7**, 418 (2010).